CANCER

The super elongation complex drives transcriptional addiction in *MYCN*-amplified neuroblastoma

Donghai Wang[1,2]†, Zhinang Yin[3]†, Honghong Wang[3]†, Liyuan Wang[2], Tianyu Li[3], Ruijing Xiao[3,4], Ting Xie[2], Ruyi Han[2], Rui Dong[5], Hudan Liu[2]*, Kaiwei Liang[3,6]*, Guoliang Qing[1,2,6]*

***MYCN* amplification in neuroblastoma leads to aberrant expression of MYCN oncoprotein, which binds active genes promoting transcriptional amplification. Yet, how MYCN coordinates transcription elongation to meet productive transcriptional amplification and which elongation machinery represents MYCN-driven vulnerability remain to be identified. We conducted a targeted screen of transcription elongation factors and identified the super elongation complex (SEC) as a unique vulnerability in *MYCN*-amplified neuroblastomas. MYCN directly binds EAF1 and recruits SEC to enhance processive transcription elongation. Depletion of EAF1 or AFF1/AFF4, another core subunit of SEC, leads to a global reduction in transcription elongation and elicits selective apoptosis of *MYCN*-amplified neuroblastoma cells. A combination screen reveals SEC inhibition synergistically potentiates the therapeutic efficacies of FDA-approved BCL-2 antagonist ABT-199, in part due to suppression of MCL1 expression, both in *MYCN*-amplified neuroblastoma cells and in patient-derived xenografts. These findings identify disruption of the MYCN-SEC regulatory axis as a promising therapeutic strategy in neuroblastoma.**

INTRODUCTION

Neuroblastoma is the most common extracranial childhood cancer, which accounts for ~15% of pediatric cancer-related mortality. Low- and intermediate-risk diseases are mostly curable, yet the high-risk neuroblastomas have a poor prognosis (*1*). *MYCN* amplification occurs in ~50% of high-risk neuroblastomas and contributes to a large percentage of therapy resistance and cancer-related deaths (*2*). The lack of effective treatment continues to be a major clinical challenge for the antineoplastic therapy of *MYCN*-amplified neuroblastoma.

MYCN belongs to a family of oncogenes, which in addition to *MYCN*, includes two closely related genes, *MYC* and *MYCL* (*3*, *4*). Amplification of the *MYCN* gene is predominantly found in neuroendocrine tumors, including neuroblastoma, medulloblastomas, and neuroendocrine prostate cancer. *MYCN* amplification is an initiating event driving the development of high-risk neuroblastoma. Targeted MYCN overexpression in peripheral neural crest is sufficient to initiate disease in mouse models (*5*), while MYCN inhibition broadly reverses tumor stem–like phenotypes and aberrant proliferation (*6*). Hence, therapeutic strategies to indirectly target MYCN expression or protein stability have reduced tumor growth in preclinical tumor models (*7*–*9*).

The MYC family oncoproteins are "super-transcription factors" that drive a robust transcriptional response involved in almost every aspect of tumorigenesis. Both MYC and MYCN have been found to broadly remodel the cancer cis-regulatory landscape together with RNA polymerase II (Pol II), leading to global transcriptional amplification (*10*, *11*). Transcription starts with the recruitment of Pol II to core promoters in the context of chromatin (*12*, *13*). A short transcript is produced by Pol II and pause factors typically induce pausing 20 to 50 bp downstream of the transcriptional start site. Productive elongation requires the assembly of a highly processive and fast transcriptional apparatus. Elongation proceeds after the elongation factor positive transcription elongation factor b (P-TEFb), which consists of CDK9 and cyclin T, is recruited, and phosphorylates at least three targets important for transcriptional control: the suppressor of Ty 5 homolog subunit of 5,6-dichloro-1-β-D-ribofuranosylbenzimidazole sensitivity–inducing factor, the negative elongation factor complex member E , and the serine 2 of Pol II C-terminal domain (*14*). MYC was previously shown to stimulate recruitment of the elongation factor P-TEFb and thus transcription elongation (*15*), while MYCN was reported to use breast cancer 1 and nuclear exosome complex to ensure proper transcription termination (*16*, *17*).

Yet the precise nature and the molecular mechanisms underlying MYCN-driven transcriptional elongation remain elusive. In particular, which elongation machinery represents MYCN-driven vulnerability remain to be identified.

In this study, we used MYCN-driven neuroblastomas as model systems and identify that MYCN-directed elongation is particularly addicted to the super elongation complex (SEC). MYCN directly binds EAF1 and recruits SEC to ensure productive transcription elongation. EAF1 depletion, which disrupts MYCN-SEC interaction, leads to a marked reduction in transcription elongation and elicits selective apoptosis of *MYCN*-amplified neuroblastoma cells. These findings provide a mechanistic insight into MYCN-driven transcription elongation, nominating disruption of the MYCN-SEC regulatory axis as a promising therapeutic strategy in neuroblastoma.

[1]Department of Urology, Medical Research Institute, Zhongnan Hospital of Wuhan University, Wuhan University, Wuhan 430071, China. [2]Frontier Science Center for Immunology and Metabolism, Wuhan University, Wuhan 430071, China. [3]Department of Pathophysiology, School of Basic Medical Sciences, Wuhan University, Wuhan 430071, China. [4]Department of Immunology, School of Basic Medical Sciences, Wuhan University, Wuhan 430071, China. [5]Department of Pediatric Surgery, Children's Hospital of Fudan University and Shanghai Key Laboratory of Birth Defects, Shanghai 201102, China. [6]Taikang Center for Life and Medical Sciences, Wuhan University, Wuhan 430071, China.
†These authors contributed equally to this work.
*Corresponding author. Email: qingguoliang@whu.edu.cn (G.Q.); kwliang@whu.edu.cn (K.L.); hudanliu@whu.edu.cn (H.L.)

RESULTS

Identification of SEC as an essential machinery for MYCN-driven transcription elongation

We exploited SHEP MYCN-ER (*18*), a *MYCN* single-copy neuroblastoma cell line bearing a 4-hydroxytamoxifen (4-OHT)–activating *MYCN* transgene, to investigate MYCN-driven transcriptional output (Fig. 1A). Consistent with previous findings (*16*), RNA sequencing (RNA-seq) analysis using spike-in normalization showed that activation of MYCN induced a time-dependent transcriptional response with increasing numbers of differentially expressed genes [$\log_2$ fold change (FC) > 0.5 and FDR (false discovery rate) < 0.05] (fig. S1A). We next performed transient transcriptome sequencing (TT-seq) coupled with 4-thiouridine (4sU) to investigate the impact of MYCN on nascent RNA synthesis (Fig. 1B). As shown in the metagene plots of TT-seq signals throughout the gene body, MYCN activation markedly increased 4sU-labeled RNA production (Fig. 1C). MYCN induction led to increased TT-seq signals downstream of the transcription end sites (fig. S1B). On the basis of the torpedo model of transcription termination whereby kinetic competition between Pol II elongation and exonuclease activities determines the termination site (*19*), these results suggest that MYCN activation leads to a genome-wide enhancement of transcription elongation, as exemplified at two MYCN classical target genes *NCL* and *NPM1* (Fig. 1D).

To determine whether any individual elongation factor predominates MYCN-driven transcription and consequently tumor cell survival, we performed a targeted screen of sixteen well-known elongation factors in SHEP MYCN-ER cells (*14*, *20*). These factors were individually depleted using the CRISPR-Cas9 system to identify the key factor(s) linked to MYCN-driven vulnerability (Fig. 1E and fig. S1C). We observed that depletion of CDK9 or SPT6 induced substantial SHEP cell death upon MYCN induction (Fig. 1E), confirming prior findings that these elongation factors play important roles in MYCN-driven tumors (*21*, *22*). However, depletion of these factors also caused marked cell death in the absence of MYCN induction. When comparing the magnitude before and after MYCN induction, three SEC components ELL associated factor 1 (EAF1), AF4/FMR2 family member 1 (AFF1), and AF4/FMR2 family member 4 (AFF4) emerged as top hits that induced most profound cell death upon 4-OHT administration (Fig. 1E). In addition, depletion of GDOWN1 (also termed POLR2M, RNA polymerase II subunit M) caused a similar cell death ratio [4-OHT/dimethyl sulfoxide (DMSO)] to that of AFF4 deficiency. We therefore examined the effects of GDOWN1 on the expression of three canonical MYCN targets (*NCL*, *ODC1*, and *NPM1*) and found that GDOWN1 depletion only moderately (although statistically significant) decreased *NPM1* expression (fig. S1D). In contrast, AFF1/AFF4 depletion consistently and profoundly inhibited the expression of all three targets (fig. S1D). Given the findings that multiple subunits of SEC were enriched in the single guide RNA (sgRNA) screen and depletion of SEC subunits caused a global suppression of representative MYCN targets, we focused on SEC for further mechanistic and functional investigation. Consistently, cell viability analysis in *MYCN*-nonamplified SHEP cells and *MYCN*-amplified Kelly cells confirmed that ablation of *AFF1/4* or *EAF1* elicited selective cell death in *MYCN*-amplified Kelly cells (Fig. 1F).

Abrogation of SEC profoundly impairs MYCN-driven transcriptional activation

To examine whether SEC loss affects MYCN functions, we compared genome-wide transcription landscape in the presence or absence of functional SEC upon MYCN induction. *AFF1* and *AFF4* were knocked down by short hairpin RNA (shRNA) in SHEP MYCN-ER cells, and the MYCN transcriptional program was assessed by stranded RNA-seq (Fig. 2A). A total of 2116 genes was significantly up-regulated ($\log_2$FC > 0.5 and FDR < 0.05, red dots), and 743 genes was significantly down-regulated ($\log_2$FC < −0.5 and FDR < 0.05, blue dots) upon 4-OHT activation of MYCN by 24 hours (Fig. 2B, left). Notably, MYCN induction of these genes was greatly attenuated upon depletion of *AFF1*/*AFF4* (Fig. 2B, right). A majority of MYCN induced genes (~78%, cluster 1, 1651 genes) were deregulated (Fig. 2C), suggesting that *AFF1*/*AFF4* knockdown significantly altered MYCN transcriptional landscape. Expression of ~22% of MYCN-activated genes (cluster 2, 465 genes) was not decreased or even slightly increased in *AFF1*/*4* knockdown cells. Conceivably, activation of this gene cluster may depend on P-TEFb or BRD4-P-TEFb rather than SEC-P-TEFb, and *AFF1*/*AFF4* depletion could render more P-TEFb available for their induction. The effect of SEC depletion on MYCN activity is evident at two well-characterized MYCN targets, *NCL* and *NPM1* (Fig. 2D). Gene ontology analysis of cluster 1 genes revealed that these genes are mainly enriched for ribonucleoprotein complex biogenesis, ribosome biogenesis, mitochondrial gene expression, and cell cycle (Fig. 2E), indicating that SEC-dependent genes are essential for macromolecule synthesis and cell cycle progression. We further validated the essential role of SEC in MYCN target gene expression in SHEP MYCN-ER and *MYCN*-amplified Kelly cells. Quantitative polymerase chain reaction (qPCR) analysis confirmed that SEC ablation alleviated the expression of canonical MYCN targets (Fig. 2, F and G). Together, these data demonstrate the dependency of SEC activity in MYCN-mediated transcriptional activation.

EAF1 directly binds MYCN and is essential for MYCN-mediated SEC recruitment

The findings that MYCN-driven transcriptional activation is dependent on SEC propelled us to assess whether MYCN and SEC colocalize genome wide. Heatmap and boxplot analysis of chromatin immunoprecipitation sequencing (ChIP-seq) signal revealed that MYCN activation markedly increased the genomic occupancy of MYCN and the SEC subunits AFF1 and AFF4 upon 4-OHT induction of MYCN for 5 hours, concomitant with enhanced recruitment of MYC binding partner MAX (Fig. 3, A and B). Note that 4-OHT treatment for 5 hours exhibited minimal effect on AFF1 and AFF4 protein levels (fig. S2A), arguing that increased AFF1/AFF4 ChIP-seq signals upon 4-OHT treatment at this time point is predominantly due to MYCN-mediated recruitment rather than increased protein abundance. On the basis of these results, we hypothesized that SEC physically associates with MYCN to promote transcription elongation. To test this notion, we performed proximity labeling in 293T cells with MYCN-TurboID and mass spectrometry analysis to map the MYCN proximal proteins. Proteomic data show that most SEC components (CDK9, CCNT1, AFF1, AFF4, ENL, and EAF1) were identified (Fig. 3C). We next conducted coimmunoprecipitation and mass spectrometry to detect MYCN binding partners and revealed CCNT1, CDK9, and EAF1 in association with MYCN

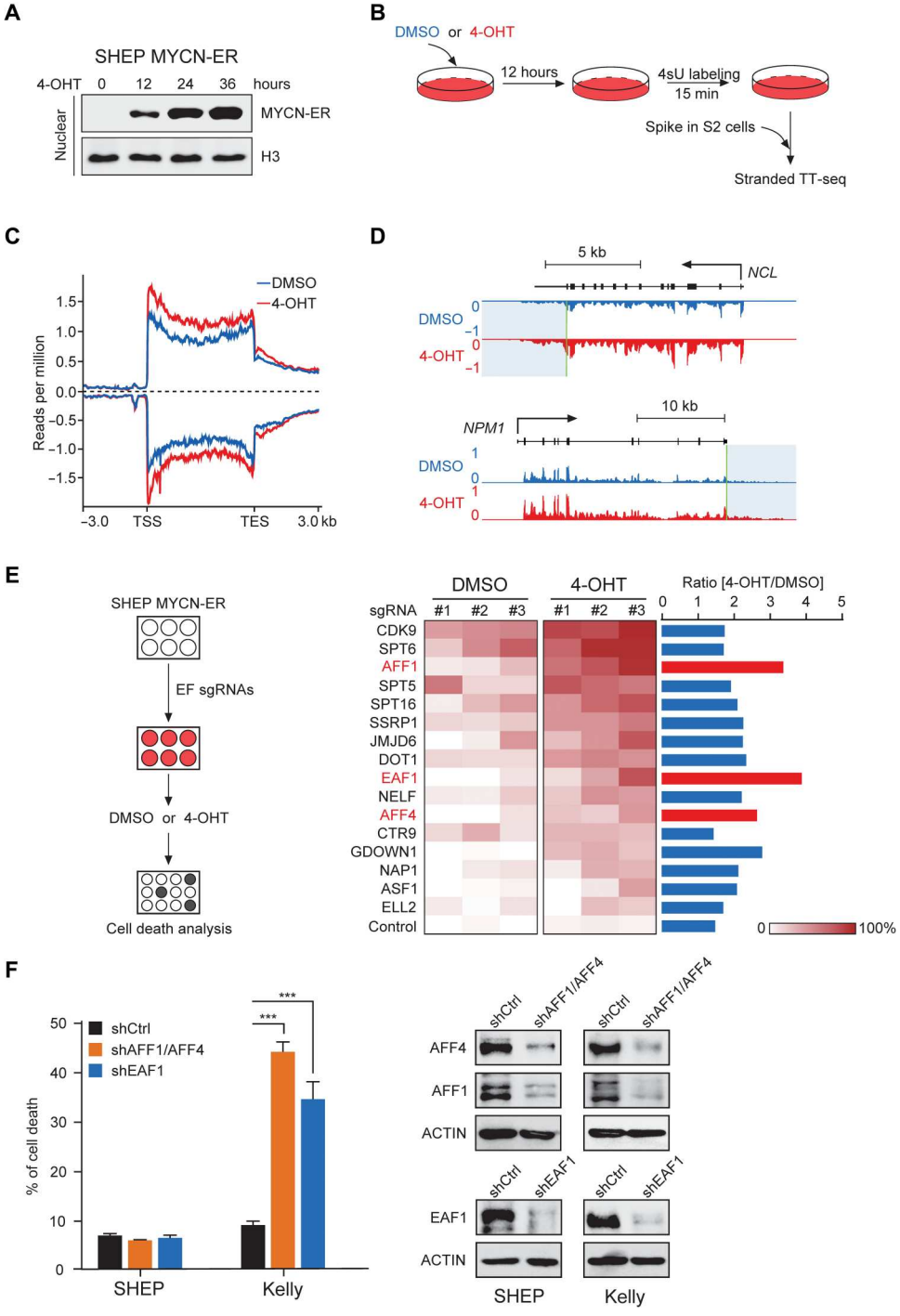

Fig. 1. Identification of the SEC as a dependency factor in MYCN-driven neuroblastoma. (**A**) Immunoblots of nuclear MYCN in SHEP MYCN-ER cells upon 4-OHT (100 nM) treatment for the indicated time points. Histone H3 was used as a loading control. (**B**) Workflow of 4sU-labeled TT-seq. SHEP MYCN-ER cells were pretreated with DMSO or 4-OHT (100 nM) for 12 hours before being refed with fresh medium containing 400 μM 4sU for 15 min. After spike-in of 4sU-labeled S2 cells, RNA was extracted and subjected to stranded TT-seq. (**C**) Metaplot of TT-seq signals of the plus and minus strands in DMSO- and 4-OHT–treated cells. (**D**) Genome browser tracks of TT-seq signals at the *NCL* and *NPM1* loci upon DMSO and 4-OHT treatment. (**E**) Targeted screen of elongation factor (EF) dependency in SHEP MYCN-ER cells (left). A total of sixteen elongation factors was individually depleted by the CRISPR-Cas9 with three single guide RNAs (sgRNAs) for each gene. Cell death was analyzed by propidium iodide (PI)–annexin V staining after 4-OHT or DMSO treatment for 72 hours (right). Heatmap visualization of the cell death upon depletion of each elongation factor and the ratio of cell death (4-OHT/DMSO) are shown on the right. (**F**) *AFF1* and *AFF4* were knocked down to fully disrupt SEC, and *EAF1* were depleted by shRNA in Kelly and SHEP cells. Kelly and SHEP cells were infected for 2 days and selected by puromycin, before Western blotting to AFF1, AFF4, and EAF1 proteins. Cell death analysis was performed at day 4 after infection. One-way analysis of variance (ANOVA) followed by Bonferroni correction was performed in (F). ***$P < 0.001$. TSS, transcription start sites; TES, transcription end sites.

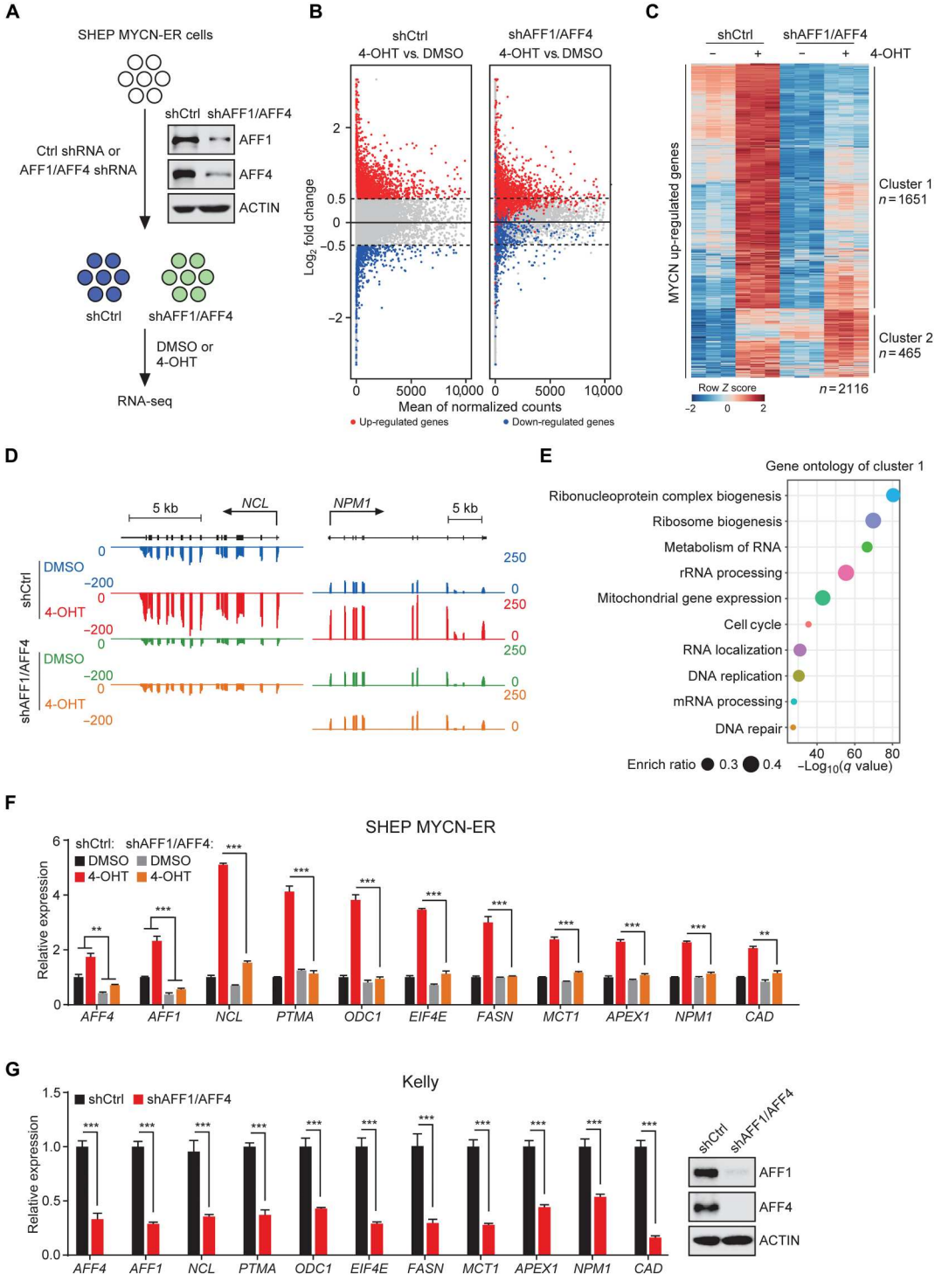

Fig. 2. SEC is required for MYCN-dependent transcriptional programs. (**A**) Experimental design for depletion of SEC in SHEP MYCN-ER cells followed by DMSO or 4-OHT treatment and RNA-seq. SHEP MYCN-ER cells were infected with lentiviruses expressing control (Ctrl) or *AFF1* and *AFF4* shRNA for 48 hours. Gene expression pattern of SHEP MYCN-ER cells with or without SEC knockdown were analyzed by RNA-seq 24 hours after 4-OHT (100 nM) or DMSO treatment. (**B**) MA-plots showing 4-OHT significantly changed genes (FDR < 0.05, $\log_2$FC > 0.5) expression in control (left) and SEC knockdown group (right). Significant up-regulated and down-regulated genes are shown as red and blue dots, respectively. (**C**) Heatmap clustering of up-regulated genes in SHEP MYCN-ER cells with the indicated treatments. Rows show *Z* scores calculated for each vector. *n* indicates the number of genes. (**D**) Genome browser views of RNA-seq raw reads at the *NCL* and *NPM1* loci. (**E**) Gene ontology analysis of genes in cluster 1. Gene ontology analysis was performed with Metascape (http://metascape.org/). rRNA, ribosomal RNA. (**F** and **G**) Quantitative reverse transcription polymerase chain reaction (qRT-PCR) validation of representative MYCN target genes in SHEP MYCN-ER cells (F) and Kelly cells (G) upon indicated treatment. SHEP MYCN-ER cells were treated with 4-OHT for 24 hours in (F). One-way ANOVA followed by Bonferroni correction was used in (F), and unpaired two-tailed Student's *t* test was used in (G). $^{**}P < 0.01$ and $^{***}P < 0.001$.

(Fig. 3C). In vitro glutathione *S*-transferase (GST) pull-down assay with recombinant GST-CCNT1, GST-CDK9, and GST-EAF1 together with His-tagged MYCN proteins demonstrated that MYCN directly binds to EAF1 with the highest affinity (Fig. 3D). Interaction between endogenous MYCN and EAF1 was validated in two *MYCN*-amplified Kelly and NLF cells (Fig. 3E). We also observed a mild protein interaction between MYCN and CDK9, consistent with previous reports suggesting MYC association with CDK9 (*15*).

Given that EAF1 is preferentially required for the survival of MYCN-driven SHEP cells (Fig. 1E) and EAF1 directly binds to MYCN, we tested whether EAF1 orchestrates the genome-wide recruitment of SEC for MYCN-directed transcription. ChIP-seq analysis showed that depletion of EAF1 failed to recruit AFF1 and AFF4

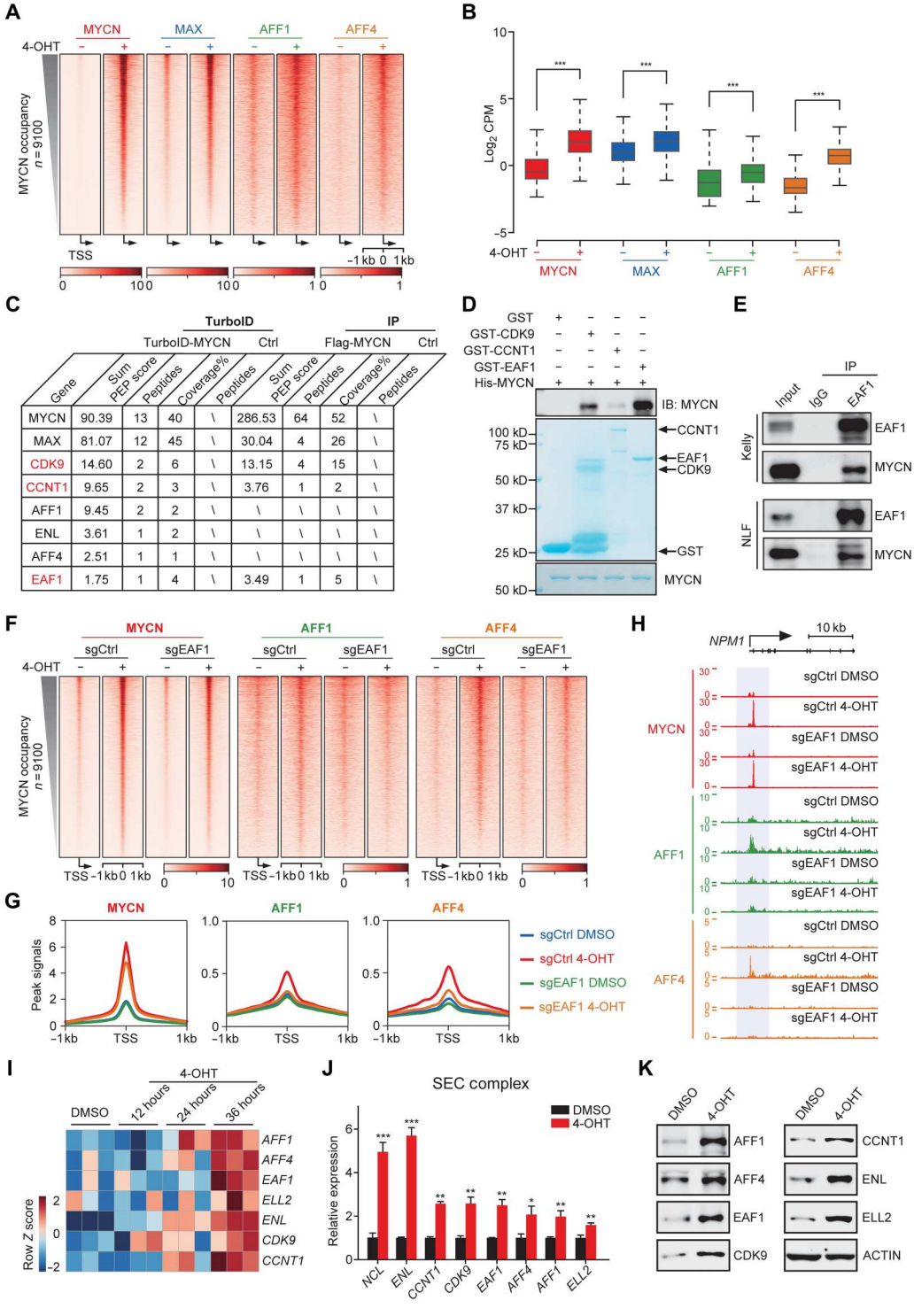

Gene	TurboID-MYCN Sum PEP score	TurboID-MYCN Peptides	TurboID-MYCN Coverage%	TurboID-MYCN \	Ctrl Peptides	Flag-MYCN Sum PEP score	Flag-MYCN Peptides	Flag-MYCN Coverage%	Ctrl \	Ctrl Peptides
MYCN	90.39	13	40	\	286.53	64	52	\		
MAX	81.07	12	45	\	30.04	4	26	\		
CDK9	14.60	2	6	\	13.15	4	15	\		
CCNT1	9.65	2	3	\	3.76	1	2	\		
AFF1	9.45	2	2	\	\	\	\	\		
ENL	3.61	1	2	\	\	\	\	\		
AFF4	2.51	1	1	\	\	\	\	\		
EAF1	1.75	1	4	\	3.49	1	5	\		

Fig. 3. MYCN interacts with EAF1 and globally recruits SEC to target genes. (**A**) ChIP-seq analysis of MYCN, MAX, AFF1, and AFF4 occupancies at the MYCN-binding promoter peaks ($n = 9100$) in SHEP MYCN-ER cells treated with 4-OHT or DMSO for 5 hours. Heatmaps show ChIP-seq signal in a window of ±1 kb centered at the peaks of MYCN. (**B**) Box plot analysis of occupancy signals showing the $\log_2$ counts per million of MYCN, MAX, AFF1, and AFF4 ChIP-seq with or without 4-OHT treatment. *P* values were calculated by the Wilcoxon test. (**C**) 293T cells expressing MYCN-TurboID or Flag-MYCN were applied for TurboID or co-IP mass spectrometry analysis. The sum posterior error probability (PEP) score corresponds to the score calculated based on the PEP values of the peptide spectrum matches. (**D**) Purified recombinant GST-CDK9, CCNT1, or EAF1 proteins coupled to GST beads were used to pull down His-MYCN, followed by immunoblotting using the MYCN antibody. Coomassie blue staining of input proteins is shown at the bottom. IB, immunoblotting. (**E**) Co-IP with EAF1 antibody to detect MYCN in Kelly and NLF cell lysates. IgG, immunoglobulin G. (**F** and **G**) Heatmap (F) and metaplot (G) of MYCN, AFF1, and AFF4 occupancies at the MYCN-binding promoter peaks [$n = 9100$, as shown in (A)] in EAF1-depleted SHEP MYCN-ER cells treated with 4-OHT or DMSO for 5 hours. (**H**) ChIP-seq signals of MYCN, AFF1, and AFF4 at the *NPM1* locus are shown. (**I**) Heatmap visualization of SEC component expression changes in SHEP MYCN-ER cells upon 4-OHT treatment. (**J** and **K**) qPCR analysis (J) and immunoblots (K) of SEC components in SHEP MYCN-ER cells upon 4-OHT treatment for 24 hours. Unpaired two-tailed Student's *t* test was used in (J). $^*P < 0.05$, $^{**}P < 0.01$, and $^{***}P < 0.001$.

to chromatin upon 4-OHT induction, although the MYCN binding to chromatin was largely unaffected (Fig. 3, F and G). This can be exemplified by genome browser views of *NPM1* and *NCL* (Fig. 3H and fig. S2B). Notably that the protein levels of AFF1, AFF4, CDK9 and cyclin T remained unaltered upon EAF1 depletion (fig. S2C), suggesting that EAF1 deficiency is not affecting the SEC integrity. A longer 4-OHT induction of MYCN also activated the expression of multiple SEC components (Fig. 3, I to K), suggesting that MYCN and SEC constitute a feed-forward activation loop to potentiate MYCN-driven transcriptional amplification. Together, these data delineate a mechanism underlying SEC dependency in MYCN-driven transcription elongation and demonstrate that EAF1 functions as a bridge that orchestrates the functional link between MYCN and SEC.

EAF1 depletion attenuates MYCN-driven transcription elongation

We next performed ChIP-seq of RNA Pol II phosphorylated at Ser2 (Pol II S2P) to examine the occupancy at MYCN targets. As expected, 4-OHT induction markedly increased Pol II S2P occupancy at MYCN–up-regulated genes, which were otherwise attenuated upon EAF1 depletion (Fig. 4, A and B, and fig. S3A). To directly evaluate the EAF1 function in MYCN-mediated transcription elongation, we used RNA-seq in SHEP MYCN-ER cells treated with a flavopiridol (FP)–induced pause, followed by release in the presence of 4sU (4sU-FP-seq) (Fig. 4C). As shown in Fig. 4D and fig. S3B, the distance that Pol II traveled after release was markedly increased upon 4-OHT activation of MYCN induction, and EAF1 loss significantly reduced Pol II travelling and processive transcription elongation. Genome browser snapshots further confirmed a marked attenuation of Pol II elongation at the MYCN target *NPM1* (Fig. 4E).

As direct pharmacological targeting of EAF1 is currently unavailable, we used the small-molecule KL-2, which disrupts the interaction between AFF1/4 and P-TEFb and thus inhibits SEC assembly (*23*), as an alternative. Similar to the effect of SEC depletion shown in Fig. 2C, KL-2 treatment led to over 85% of MYCN-activated genes being deregulated (2137 genes, cluster 3 versus 372 genes, cluster 4) (fig. S3C). The SEC-dependent MYCN targets (cluster 1; Fig. 2C) were largely overlapped with the KL-2–suppressed genes (cluster 3) (fig. S3D). Moreover, 4sU-FP-seq analysis demonstrated that KL-2 significantly attenuated MYCN-driven Pol II travelling and processive transcription elongation (Fig. 4F and fig. S3E), which was also evident in genome browser views of the canonical MYCN targets *NPM1* and *NCL* (Fig. 4G and fig. S3F). These data reveal that disruption of SEC by KL-2 similarly suppressed MYCN target gene expression and faithfully recapitulated the transcriptional defect resulting from EAF1 depletion.

Coinhibition of SEC and BCL-2 exhibits synergistic lethality in *MYCN*-driven neuroblastoma cells

Given the prominent role of SEC in MYCN-dependent transcription, we reasoned that MYCN-driven neuroblastomas are particularly sensitive to KL-2 treatment. Administration of KL-2 led to selective apoptotic cell death in 4-OHT–treated SHEP MYCN-ER cells as well as in *MYCN*-amplified Kelly, BE-2C, and NLF cells (Fig. 5, A and B). It was further evident that KL-2 treatments markedly inhibited Kelly xenograft tumor progression with minimal effect on the mouse body weight (Fig. 5C and fig. S4, A to C).

To potentiate the cytotoxic activity of KL-2, we conducted a drug combination screen in Kelly cells. The drug library consists of 1430 Food and Drug Administration (FDA)–approved and clinical trial drugs. The most synergistic hits were defined as compounds exhibiting more than fourfold toxic effects in combination treatment compared to KL-2 alone (Fig. 5D). Venetoclax (also termed ABT-199), pracinostat, fludarabine, regorafenib, and mubritinib emerged at the top five hits (Fig. 5E). We validated these results in annexin V staining assays, and ABT-199 manifested the strongest synergism with KL-2 (fig. S4D). It is notable that previous studies have reported that B-cell lymphoma 2 (BCL-2) is a promising therapeutic target in neuroblastoma (*24*). This coinhibitory strategy was selective to induce tumor cell death in *MYCN*-overexpressing neuroblastoma cells, as shown in 4-OHT–treated SHEP MYCN-ER cells as well as *MYCN*-amplified cell lines (Kelly, BE-2C, and NLF) and primary tumor cells from neuroblastoma patients (#1 and #2) (Fig. 5F and fig. S4, E and F). The drug combination indices (CI) were less than 1 in *MYCN*-amplified cells but over 1 in the *MYCN* nonamplified one (Fig. 5G), suggesting that the synergistic efficacy is dependent on the *MYCN* genetic status.

We tested BCL-2 expression and several pro- or anti-apoptotic proteins in response to KL-2 treatment and found that only myeloid cell leukemia 1 (MCL1) was down-regulated in Kelly cells (Fig. 5H). As decrease of MCL1 sensitizes tumor cells to BCL-2 inhibition, these results provide a mechanistic basis for synergistic cell death by dual KL-2 and ABT-199 treatments. Notably, KL-2–mediated MCL1 down-regulation was only detected in *MYCN*-amplified (Kelly, BE-2C, and NLF) but not nonamplified ones (SHEP) (Fig. 5I). Enforced MCL1 expression desensitized Kelly cells to cotreatment (Fig. 5J and fig. S4G). To explore the mechanism underlying KL-2–mediated MCL1 down-regulation, we depleted *MYCN* or *AFF1/4* in Kelly cells individually and found that *MCL1* mRNA and protein levels were reduced, consistent with the findings upon pharmacological inhibition of SEC by KL-2 (fig. S5, A to E). Moreover, genome browser tracks of ChIP-seq showed that MYCN and AFF1/4 occupied the *MCL1* promoter (fig. S5F), supporting *MCL1* as a direct transcriptional target of both MYCN and SEC. In addition, 4sU-FP-seq upon KL-2 treatment and UCSC genome browser snapshots at the *MCL1* loci showed reduced Pol II traveling, demonstrating that KL-2 attenuates *MCL1* transcription elongation (fig. S5G). These results support the notion that decreased MCL1 is a prominent mechanism responsible for the observed drug synergy between KL-2 and ABT-199.

KL-2 and ABT-199 synergistically inhibit neuroblastoma growth in vivo

To examine the functional consequences of pharmacological inhibition of SEC and BCL-2 in vivo, we exploited Kelly xenografts for dual treatment. As shown in Fig. 6A, treatment of KL-2 or ABT-199 alone suppressed tumor growth, and the combination treatment led to a more pronounced inhibition. Xenograft tumors were excised after 14-day treatment, and the cotreatment group exhibited substantially smaller tumors (Fig. 6B). We further evaluated therapeutic efficacy in patient-derived xenografts (PDXs) derived from primary *MYCN*-amplified neuroblastoma cells (primary #1 in Fig. 5F). Treatment started at the day 25 after implantation when the xenograft tumors reached about 200 mm^3 and lasted for 14 days. We monitored the tumor growth every other day, and mice were euthanized when the tumor size reached 2000 mm^3. As shown in Fig. 6 (C and D), drug combination synergistically suppressed MYCN-driven neuroblastoma growth in comparison to the single treatment and significantly extended survival of recipient mice. Immunohistochemistry (IHC) staining confirmed that cotreatment suppressed tumor cell proliferation and induced intratumoral cell apoptosis in the PDX tumors, evidenced by reduced proliferating cell nuclear antigen (PCNA) and enhanced cleaved caspase-3 staining (Fig. 6, E and F). Notably, drug combination elicited tolerable toxic effects, leading to minimal changes in body weights of Kelly or PDXs (fig. S6, A and B). We also evaluated the toxicity of the drug combination in healthy wild-type mice using the same treatment strategy as shown in Fig. 6A. Dual treatments caused minimal overall changes in hematopoietic cell numbers, liver and kidney function parameters despite a moderate decrease in white blood cells (fig. S6, C and D). As a result, this treatment modality holds

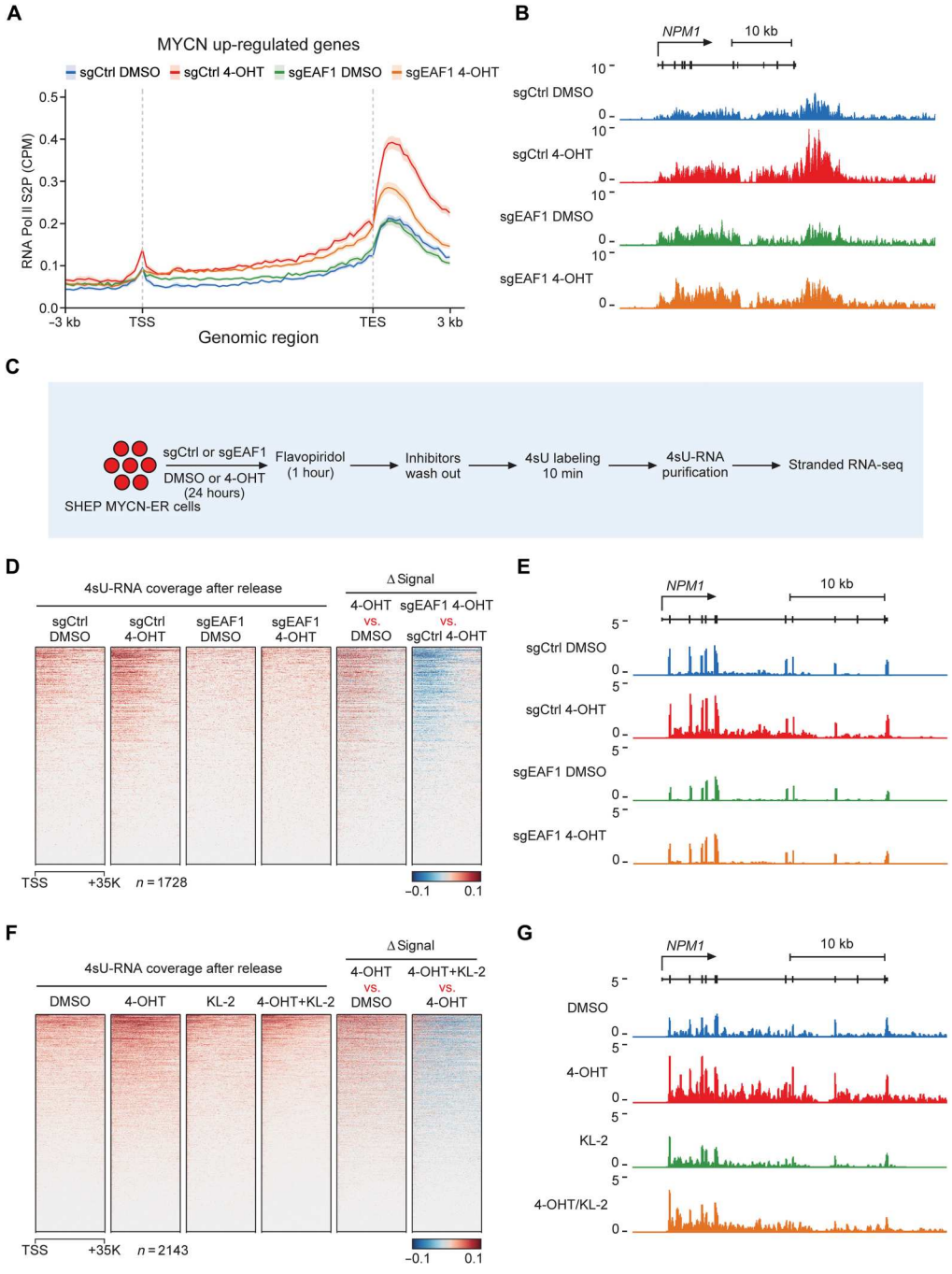

Fig. 4. SEC primarily mediates MYCN-dependent transcription elongation through EAF1. (**A**) Metagene plots of Pol II S2P in MYCN-activated genes ($n = 2116$). SHEP MYCN-ER cells with or without EAF1 depletion were, respectively, treated with 4-OHT or DMSO for 5 hours. (**B**) Representative genome browser tracks of Pol II S2P ChIP-seq signals at the *NPM1* loci with or without EAF1 depletion. (**C**) Workflow of 4sU-FP-seq–based measurement of transcription elongation in SHEP MYCN-ER cells. Cells with or without EAF1 knockout were treated with DMSO or 4-OHT for 24 hours before addition of FP (CDK9 inhibitor, 10 μM) to pause Pol II at the promoter. Flavopiridol was then washed out, followed by 4sU labeling for 10 min. The 4sU-labeled RNA was purified for RNA-seq. (**D**) Heatmap visualization of 4sU-FP-seq signals in DMSO- or 4-OHT–treated cells and changes of 4sU-FP-seq signal upon EAF1 knockout. All genes up-regulated by 4-OHT were plotted using the total 4sU-FP-seq signals. (**E**) Genome browser views of 4sU-FP-seq analysis at the *NPM1* loci. (**F**) Heatmap analysis of 4sU-FP-seq in DMSO- or KL-2–treated SHEP MYCN-ER cells in the presence or absence of 4-OHT (24 hours). (**G**) Genome browser tracks of 4sU-FP-seq at the *NPM1* locus with indicated treatments.

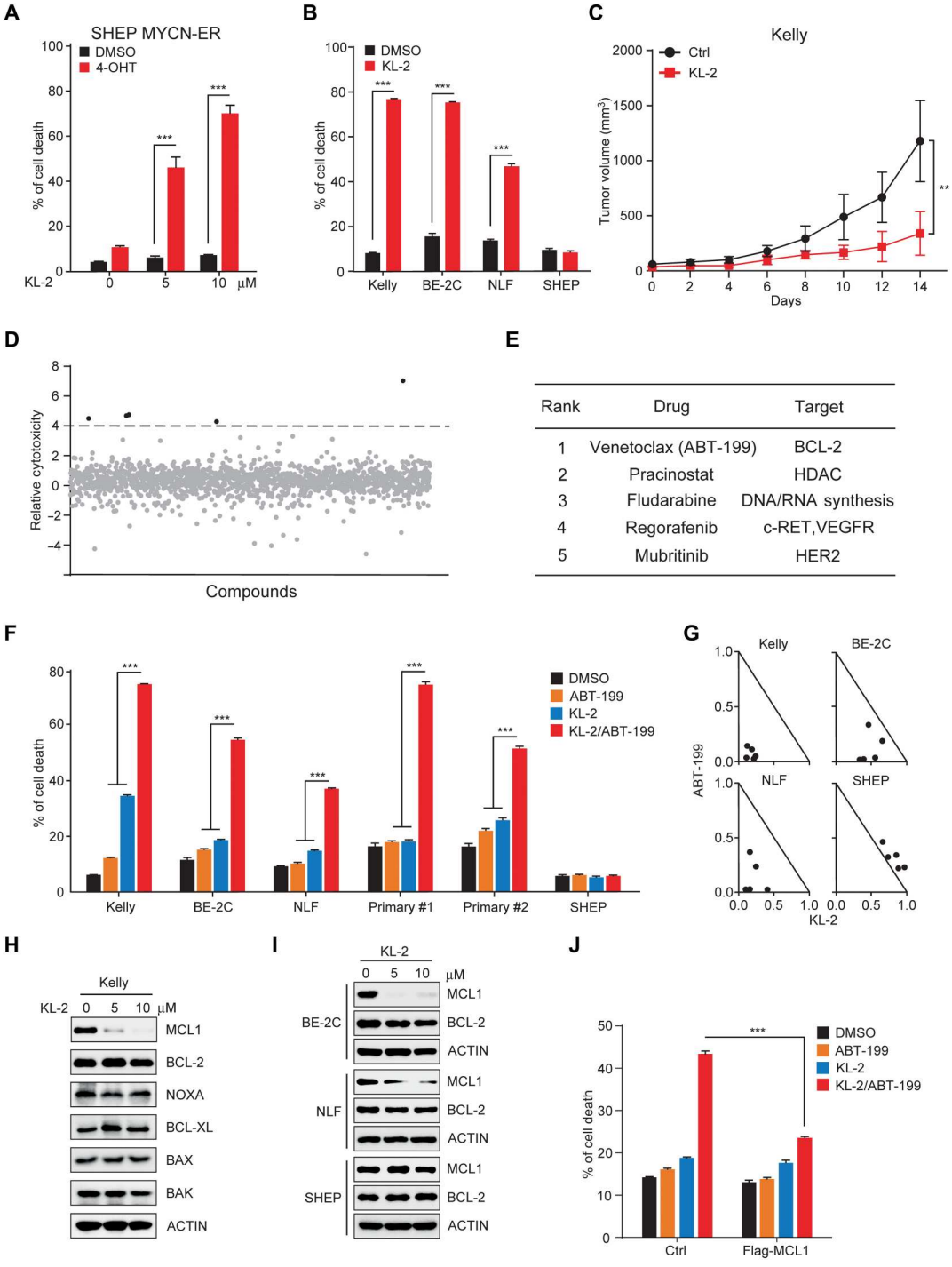

Fig. 5. ABT-199 synergizes with KL-2 to induce *MYCN*-amplified neuroblastoma cell death. (**A**) Analysis of KL-2–mediated cell death in SHEP MYCN-ER cells pretreated with or without 4-OHT (100 nm) for 24 hours. (**B**) Cell death analysis of neuroblastoma cells treated with KL-2 (10 μM). (**C**) Kelly xenograft tumor growth after 2-week treatment with vehicle (corn oil) and KL-2 (50 mg/kg). Six tumors were analyzed in each group. (**D** and **E**) High-throughput screening of clinically used drugs in Kelly cells to identify small molecules synergistic with KL-2 (D). Top hits are listed in (E). HDAC, histone deacetylase; c-RET, ret proto-oncogene; VEGFR, vascular endothelial growth factor receptor; HER2, human epidermal growth factor receptor 2. (**F**) Cell death analysis of neuroblastoma cell lines and primary human patient cells (with *MYCN* amplification) treated with KL-2 (5 μM) and/or ABT-199 (5 μM). (**G**) Combination index (CI) of KL-2 and ABT-199 was calculated using the CalcuSyn software (Biosoft). (**H**) Immunoblotting for several BCL-2 family proteins in Kelly cells upon KL-2 treatment. (**I**) Immunoblots of MCL1 and BCL-2 with or without KL-2 treatment for 24 hours in neuroblastoma cell lines. (**J**) Kelly cells expressing MCL1 were subjected to KL-2 (2.5 μM), ABT-199 (5 μM), or combination treatment, followed by cell death analysis. Unpaired two-tailed Student's *t* test was used in (A) to (C). One-way ANOVA followed by Bonferroni correction was used in (F), and two-way ANOVA was used with Bonferroni correction in (J). ***$P < 0.001$.

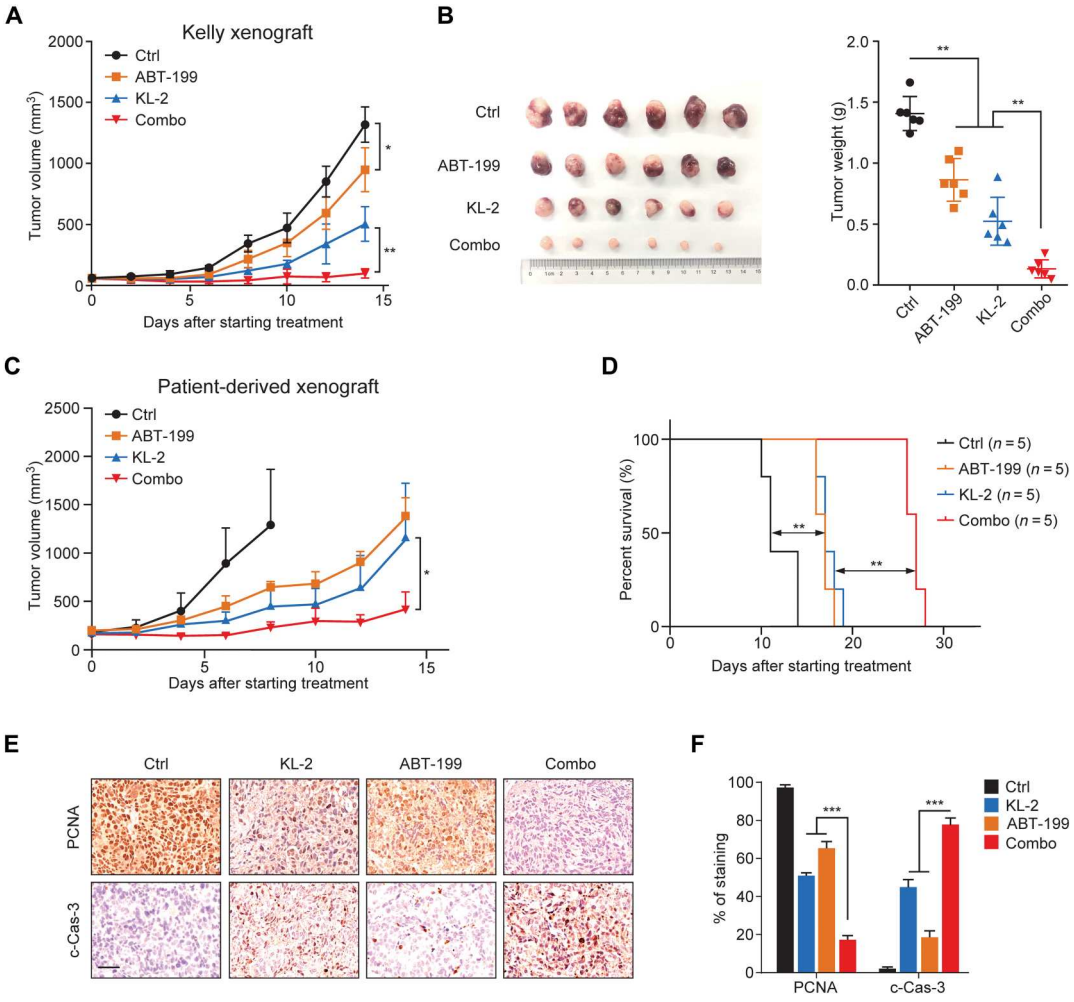

Fig. 6. KL-2 and ABT-199 synergistically suppress *MYCN*-mediated neuroblastoma in vivo. (**A** and **B**) Tumor growth in Kelly xenografts treated with vehicle, KL-2 (25 mg/kg), ABT-199 (20 mg/kg), or in combination ($n = 6$ for each group) (A). Tumor images and weights at the 14th day after treatment are shown (B). (**C** and **D**) *MYCN*-amplified neuroblastoma patient-derived tumor samples were transplanted into NPG mice. Tumor growth of PDXs treated with vehicle, KL-2 (25 mg/kg), ABT-199 (20 mg/kg), or in combination for 2 weeks are shown in (C) ($n = 5$ for each group). Recipients were euthanized when the tumor size reached 2000 mm^3, and Kaplan-Meier survival curves are shown in (D). (**E** and **F**) Representative images of immunohistochemical (IHC) staining of PCNA and cleaved caspase-3 (c-Cas-3) in PDX tumors at day 10 after starting treatment (E). Scale bar, 50 μm. Quantifications are shown in (F). One-way ANOVA test followed by Bonferroni correction was used in (A) to (C) and (F). Log-rank test was used in (D) for Kaplan-Meier survival analysis. *$P < 0.05$, **$P < 0.01$, and ***$P < 0.001$.

a great translational potential for MYCN-driven high-risk neuroblastoma therapy.

DISCUSSION

Amplification of the *MYCN* oncogene predicts treatment resistance and particularly poor prognosis in childhood neuroblastoma. Effective treatment of high-risk neuroblastoma has been hampered by the predominance of the currently "undruggable" MYCN transcription factor (*4*). Attempts to directly and specifically target MYCN have failed due to the unstructured nature of MYC family proteins in their monomeric form. Approaches of targeting the MYCN-driven transcriptional programs hold great promise for neuroblastoma treatment. To this end, we screened for the most critical elongation factors that are engaged in MYCN-driven transcriptional activation. We identified SEC as a key elongation machinery for MYCN-driven transcription. Genetic and pharmacological inhibition of SEC blocks MYCN-mediated transcription amplification and selectively induces neuroblastoma cell death in vitro and in vivo (Fig. 7).

MYCN plays a major role in the control of Pol II pause release and subsequent transcription elongation. We here demonstrate that SEC primarily mediates MYCN-driven transcription elongation in neuroblastoma as approximately 80% of MYCN target genes are significantly impaired upon SEC inactivation. As a result, SEC inhibition led to robust and selective apoptosis in MYCN-induced cells. Notably, MYCN also activates the transcription of multiple SEC subunits. These findings suggest a MYCN-SEC feed-forward loop contributing to mutual high expression, leading to MYCN-driven transcriptional amplification and tumor progression.

The histone chaperone FACT (facilitates chromatin transcription) complex aids transcription elongation by remodeling

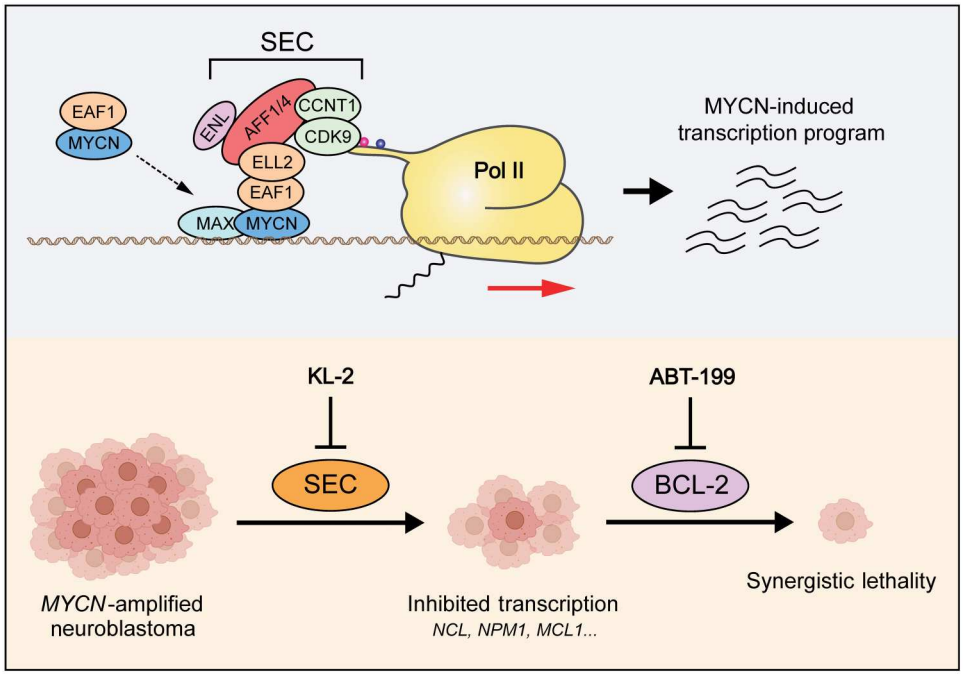

Fig. 7. Proposed mechanism for the action of SEC-mediated transcription elongation in MYCN-driven neuroblastoma cells and the mechanism-based targeted strategy. In MYCN-amplified neuroblastoma cells, overexpressed MYCN recruits SEC to chromatin through EAF1. As a consequence, SEC-loaded Pol II produces enhanced processive transcription elongation (**top**). Pharmacological inhibition of SEC by KL-2 disrupts SEC and induces selective cell death. Drug library screen identifies ABT-199 as a synergistic drug in combination with KL-2, suggesting dual inhibition of SEC and BCL-2 as a promising therapeutic strategy for high-risk neuroblastoma (**bottom**).

nucleosomes to allow for Pol II transit through the gene. FACT has been identified as a crucial mediator of the MYCN signal and a potential therapeutic target in neuroblastoma (*25*). However, the precise mechanism and implications of the FACT inhibitor CBL0137 are still not well understood, especially in terms of its specific impact on FACT-dependent transcriptional programs. Our findings here delineate a crucial mechanism that MYCN-EAF1 interaction renders the MYCN-driven tumor cells mainly depending on SEC for processive transcription elongation (Fig. 7). It remains possible that MYCN directly either recruits SEC through the MYCN-EAF1 interaction or collaborates with other factors including the mediator complex and P-TEFb to enhance SEC occupancy and transcription elongation (*15*, *26*). Nevertheless, our findings show that depletion of EAF1 reduces the SEC complex abundance at MYCN target genes and blocks transcription elongation. Accordingly, *MYCN*-amplified neuroblastoma cells mainly rely on SEC for processive transcription elongation. We therefore provide a molecular basis for applying the SEC inhibitor KL-2 to suppress neuroblastoma tumorigenesis. KL-2 has been reported to disrupt phase separation of SEC and curb transcriptional activation and has shown promise in potentiating immunotherapy in glioblastoma stem cells (*27*, *28*). Our findings here suggest *MYCN* amplification as a biomarker predicting KL-2 sensitivity.

Coinhibition of SEC and BCL-2 presents a combination treatment modality for *MYCN*-amplified high-risk neuroblastoma. Previous work suggests that BCL-2 expression is regulated by SEC in mixed lineage leukemia–fusion leukemia, yet our results suggest that BCL-2 expression is independent of SEC in both *MYCN*-amplified or *MYCN*-nonamplified neuroblastomas. Instead, the well-known anti-apoptotic factor MCL1 was markedly and specifically down-regulated by KL-2 in *MYCN*-amplified neuroblastoma, suggesting that MCL1 is an SEC target in this tumor context. Decreased MCL1 expression sensitizes tumor cells to BCL-2 inhibitor ABT-199 (*29*), a compound already approved by the FDA for treatment of chronic lymphocytic leukemia and acute myeloid leukemia. Notably, this combination strategy appears well tolerated in our mouse models. With these findings, KL-2 or more advanced SEC inhibitors, in combination with ABT-199, may serve as a promising therapy for high-risk neuroblastoma.

MATERIALS AND METHODS

Cell culture

Neuroblastoma cell lines Kelly, BE-2C, NLF, SHEP, and SHEP MYCN-ER were obtained from J. M. Maris (Children's Hospital of Philadelphia, University of Pennsylvania, Philadelphia, PA, USA). Where indicated, SHEP MYCN-ER cells were activated by 100 nM 4-OHT (Topscience, #T6743). 293T cells were purchased from American Type Culture Collection. *Drosophila melanogaster* S2 cells were provided by Y. Xu (College of Life Sciences, Wuhan University, China). Neuroblastoma cell lines were cultured in RPMI 1640 (Hyclone, #SH30809.01) medium supplemented with 10% fetal bovine serum (FBS; Gibco, #10099-141) and 1% penicillin/streptomycin (Hyclone, #S110JV). 293T cells were cultured in Dulbecco's modified Eagle's medium (DMEM; Sigma-Aldrich, #D6429) medium containing 10% FBS (Gemini, #100-500) and 1% penicillin/streptomycin. S2 cells were grown in the Schneider's insect medium (Sigma-Aldrich, #S0146) containing 10% FBS at 25°C. Human primary neuroblastoma tumor samples were obtained with informed consents from Children's Hospital of Fudan

University with patient information listed in table S1. Patient-derived primary neuroblastoma cells were grown in DME/F12 medium (Sigma-Aldrich, #D8437) containing 15% FBS, 1% nonessential amino acids (Gibco, #M7145), 2 mM L-glutamine, 1 mM sodium pyruvate, 1% B27 (Thermo Fisher Scientific, #17504044), epidermal growth factor (10 ng/ml; Sigma-Aldrich, #E9644), fibroblast growth factor (15 ng/ml; Peprotech, #100-18B-50UG), and 1% penicillin/streptomycin.

Immunoblot and immunoprecipitation

For whole-cell extraction, cells were lysed in radioimmunoprecipitation assay (RIPA) buffer [50 mM tris (pH 7.4), 150 mM NaCl, 1% NP-40, 0.5% sodium deoxycholate, and 0.1% SDS] containing protease inhibitor cocktail. For nuclei isolation and extract preparation, cells were added with lysis buffer A [10 mM Hepes (pH 7.9), 50 mM NaCl, 0.5 M sucrose, 0.1 mM EDTA, and 0.1% Triton X-100] and precipitated 2000*g* for 10 min to precipitate nuclei, which were washed in buffer B [10 mM Hepes (pH 7.9), 10 mM KCl, 0.1 mM EDTA, and 0.1 mM EGTA] and lysed in SDS–polyacrylamide gel electrophoresis (SDS-PAGE) loading buffer.

For immunoblotting, 30 to 50 μg proteins was subjected to SDS-PAGE and then transferred to polyvinylidene difluoride membrane (Bio-Rad, #1620177). Blots were first blocked with 5% fat-free milk and then incubated with primary antibodies and appropriate horseradish peroxidase–conjugated secondary antibodies. Protein signal was detected with the Clarity Western ECL Substrate (Bio-Rad, #1705061). For immunoprecipitation (IP), cells were lysed in IP buffer [50 mM tris HCl (pH 7.4), 150 mM NaCl, 1 mM EDTA, 1% NP-40, and 1 mM dithiothreitol (DTT)] at 4°C. Cell lysates with 1-mg crude extract were incubated with antibodies conjugated to Protein G beads overnight at 4°C. Primary antibodies used in this study are listed in table S2.

RNA sequencing

Total RNA was extracted from 50 million SHEP MYCN-ER cells spiked-in with 15% *Drosophila* S2 cells using TRIzol reagent (Thermo Fisher Scientific, #15596018). mRNA was purified from 1 μg of total RNA with the VAHTS mRNA capture beads (Vazyme, #N401-02) and fragmented to 200 to 500 bp size long in 2× ProtoScript II buffer (New England Biolabs, #M0368). First- and second-strand DNA synthesis and adaptor ligation were conducted using an New England Biolabs Next Ultra RNA library prep kit for Illumina. The resulting strand-specific RNA-seq libraries were subjected to 150-bp paired-end sequencing on a NovaSeq 6000. All raw fastq reads were aligned to the *Drosophila* genome (*dm6*) and human genome (*hg38*) by HISAT2 version 2.1.0, respectively. Raw read counts were normalized to RPM (reads per million) per sample and then displayed in the UCSC genome browser as bigWig-formatted coverage tracks. Read counts at indicated regions were calculated by HTSeq-count (version 0.12.3) and were provided to DEseq2 (version 1.32.0) for differential gene expression analysis. Human gene expression was normalized using *Drosophila* spiked-in genes. FDR < 0.05 and $\log_2$FC >0.5 (or < −0.5) were used to identify differentially expressed genes.

Quantitative RT-PCR

Total RNA was isolated from cells using TRIzol reagent at 4°C. Complementary DNA was synthesized from 1 μg of RNA using the ReverTra Ace qPCR reverse transcription kit (TOYOBO, #FSQ-101). ChamQ SYBR qPCR Master Mix (Vazyme, #Q311-02) was used for conducting quantitative PCR on a CFX Connect Real-Time PCR System (Bio-Rad). Primer sequences for qPCR are listed in table S3.

Transient transcriptome sequencing

Cells were labeled with 400 μM 4sU (Sigma-Aldrich, #T4509) at 37°C for 15 min before total RNA extraction with TRIzol reagent. To assess elongation rates, cells were pretreated with FP (Selleck, #S2679) for 1 hour to pause Pol II near the transcription start sites before 4sU labeling. The extracted total RNA was spiked-in with 4sU-labeled *Drosophila* S2 RNA. RNA was fragmented by 0.2 M NaOH, neutralized by 1× volume of 1 M tris-HCl (pH 6.8), and precipitated with isopropyl alcohol. One hundred micrograms of total RNA was subjected to biotinylation reaction in a total volume of 250 μl containing 10 mM Hepes (pH 7.5), 1 mM EDTA, and 5 μg of biotin-XX-MTSEA (Biotium, #90066) at room temperature for 30 min. The RNA was purified with Sera-Mag carboxylate-modified magnetic beads (Sigma-Aldrich, #GE24152105050350). The biotin-labeled RNA was further purified with the MyOne streptavidin C1 dynabeads (Thermo Fisher Scientific, #65001). 4sU-RNA was eluted with DTT and subjected to strand-specific RNA-seq library preparation before next-generation sequencing on a NovaSeq 6000. TT-seq reads were aligned to the *Drosophila* genome (*dm6*) and human genome (*hg38*) using HISAT2 version 2.1.0. The resulting reads were normalized to total reads aligned (reads per million) for each strand with deepTools (version 3.3.0). The read counts across each gene were counted with HT-seq (version 0.12.3), and DESeq2 was used for differentially gene expression analysis. Metagene plots were generated by deepTools (version 3.3.0).

Chromatin immunoprecipitation sequencing

ChIP-seq was performed as previously described (*30*). Briefly, cells were cross-linked with 1% paraformaldehyde for 10 min and were quenched with glycine for 5 min. After cell lysis, fixed chromatin was fragmented to 200- to 600-bp DNA size using a Diagenode Bioruptor Plus. DNA fragments were immunoprecipitated with indicated antibodies and Protein A/G beads (Smart-Lifesciences, #SA032100). Specific antibodies against MYCN, MAX, AFF1, and AFF4 were generated by immunization in rabbits with recombinant antigens. One to 10 ng of immunoprecipitated DNA was used for DNA library preparation. ChIP-seq raw reads were aligned to the human genome (*hg38*) with Bowtie (version 1.1.2) using default settings. Read coverage was performed with deepTools and visualized with the UCSC genome browser. Peaks were called using MACS2 (version 2.1.2) with default parameters and a *P* value cutoff at 1×10^{-5} before annotation by ChIPseeker (version 1.28.3). Heatmaps and metagene plots were generated using the computeMatrix command from deepTools and NGStools, respectively.

Mass spectrometry analysis

293T cells transfected with MYCN-TurboID or Flag-MYCN were prepared for TurboID or co-IP, respectively, followed by mass spectrometry analysis. TurboID was performed as previously described (*31*). Cells were cultured in biotin-containing DMEM medium for labeling and then lysed with RIPA lysis buffer in the presence of Benzonase (Yeasen Biotechnology, #20125ES50). After precipitation at 21,000*g* for 20 min, the supernatant was incubated with

streptavidin beads, which was blocked with 1% bovine serum albumin, at 4°C. Beads were then washed with RIPA lysis buffer containing 2 M urea, and MYCN and associated proteins were then eluted with 8 M urea. For co-IP, transduced 293T cells were lysed with buffer A [10 mM Hepes-KOH (pH 7.9), 1.5 mM $MgCl_2$, and 10 mM KCl] containing 0.3% NP-40 and protease inhibitor. Cell lysate was centrifuged for 5 min at 1300*g*, and the resulting cell pellet was resuspended with micrococcal nuclease digestion buffer [10 mM Hepes (pH 7.5),10 mM $CaCl_2$, and 1 mM $MgCl_2$] in the presence of micrococcal nuclease (Thermo Fisher Scientific, #EN0181). After centrifuging at 20,000*g*, the supernatant was incubated with Flag beads, and then MYCN and associated proteins were harvested by Tobacco Etch Virus protease digestion to remove the flag tag.

Purified proteins were digested with typsin (Promega, #V5280) and desalted with C18 columns (Thermo Fisher Scientific, #87782). The resulting peptides were analyzed by an Orbitrap Exploris 480 mass spectrometer, equipped with the FAIMS Pro interface, and an EASY-nLC system using a Hypersil GOLD C18 Selectivity High-Performance Liquid Chromatography column. To process raw files, Proteome Discoverer 2.4 was used with a four-stage searching program. The strict target FDR for peptide spectrum matches or peptides was set at 0.01, and peptides with a lower confidence than 0.01 are excluded. *q*-values are greater than 0.01 for high confidence hits and 0.05 for medium confidence hits.

Pull-down assays of recombinant proteins

GST-tagged CDK9, CCNT1, or EAF1 was cloned into pGEX-4T1 to generate recombinant proteins in the *Escherichia coli* BL21 strain upon 100 μM isopropyl-β-D-thiogalactopyranoside induction overnight. Bacteria were harvested and resuspended in binding buffer [150 mM NaCl and 10 mM tris-HCl (pH 7.5)] and then subjected to sonication followed by centrifugation. The resulting supernatants were incubated with PureCube Glutathione Agarose beads (Cube Biotech, #32105) to enrich GST-tagged proteins. For in vitro pull-down, GST protein–coupled beads were washed with the binding buffer and incubated with His-MYCN proteins (Cusabio, #CSB-YP015278HU) overnight at 4°C. Beads were then washed, and associated proteins were eluted in SDS-PAGE loading buffer and subjected to immunoblotting.

Cell death analysis

Cell death was assessed by annexin V–fluorescein isothiocyanate (FITC) and propidium iodide (PI) staining. A total of 1×10^5 cells were collected and resuspended in 100 μl of binding buffer, and 1 μl of annexin V–FITC and 2 μl PI were added to cells at room temperature for 5 min. Flow cytometry was performed on Accuri C6 (BD Biosciences) and analyzed using FlowJo software.

Lentiviral transduction

Lentiviruses were generated by transfecting 293T cells with shRNA or sgRNA constructs simultaneously with the packaging plasmids (pMD2.G and psPAX2), using Lipofectamine 2000 transfection reagent (Thermo Fisher Scientific, #11668019). Viral supernatants were collected at 48 hours after transfection and filtered through a 0.22 μM filter before use. Neuroblastoma cells were transduced with appropriate amount of viral supernatants in the presence of polybrene (8 μg/ml; Santa Cruz Biotechnology, #sc-134220). Infected cells were selected by puromycin (2 μg/ml) for at least 48 hours before additional experiments were performed.

Drug screening

The library of clinically used drugs (Selleck, L1300) was used for screening synergistic drugs with KL-2. Kelly cells were seeded at a density of 3000 cells per well in 96-well plates and then treated with KL-2 (2 μM) alone or in combination with each compound (500 nM) for 24 hours. Cell death was measured by the CellTox Green Cytotoxicity Assay kit (Promega, #G8743). Fluorescence readings were collected with an automatic microplate reader (Molecular Devices). CI values were calculated using the CalcuSyn software (Biosoft) based on the Chou-Talalay method (*32*).

Neuroblastoma mouse models

For cell line xenograft tumors, each female BALB/c nude mouse (GemPharmatech) was implanted with 4 million Kelly cells diluted in 100 μl of phosphate-buffered saline and 100 μl of Matrigel (Corning, #354234). Tumor volumes were measured every other day and determined using the equation volume = 0.5 × length × width × width. Mice were randomly assigned to each treatment group when tumor size reached 100 mm^3. For patient-derived xenografts, human primary neuroblastoma tumors were transplanted in NPG mice (Beijing Vitalstar Biotechnology). Patient tumor samples were serially transplanted in NPG mice at least twice before the experiment. Xenograft tumor slices with an average volume of 5 mm^3 were subcutaneously inoculated into the flank of 5-week-old recipients. Mice were randomly divided into four groups when tumor size reached 200 mm^3 and subjected to the treatment of vehicle (corn oil), KL-2 (25 mg/kg), ABT-199 (20 mg/kg), or KL-2/ABT-199 combination once daily for 2 weeks. Tumor volumes were measured every other day. Mice were euthanized when the tumor size exceeded 2000 mm^3 for survival analysis. All animal experiments were performed under animal ethical regulations, and the study protocol was approved by the Institutional Animal Care and Use Committee of Wuhan University.

Immunohistochemistry

IHC staining was performed using paraffin-embedded tumor sections. After deparaffinization, rehydration, and high-temperature antigen retrieval, tumor sections were incubated with specific antibodies against PCNA (Santa Cruz Biotechnology, #sc-56) or cleaved caspase-3 (Cell Signaling Technology, #9661S) and then subjected to horseradish peroxidase–linked secondary antibodies for 1 hour at room temperature. The DAB substrate kit (Servicebio, #G1212-200T) was applied for visualizing staining signals. Representative IHC images were captured with a digital pathology scanner (Leica) at the ×400 magnification.

Statistics

Statistical tests were performed with GraphPad Prism 8. *P* values were calculated by unpaired two-tailed Student's *t* test between two groups or by one-way analysis of variance (ANOVA) when comparing two groups among three or more groups. The box plots were generated with R (version 3.6.1), and *P* values were calculated by the Wilcoxon test.

Supplementary Materials

This PDF file includes:

Figs. S1 to S6
Tables S1 to S3

View/request a protocol for this paper from *Bio-protocol*.

REFERENCES AND NOTES

1. K. K. Matthay, J. M. Maris, G. Schleiermacher, A. Nakagawara, C. L. Mackall, L. Diller, W. A. Weiss, Neuroblastoma. *Nat. Rev. Dis. Primers* **2**, 16078 (2016).
2. G. M. Brodeur, R. C. Seeger, M. Schwab, H. E. Varmus, J. M. Bishop, Amplification of N-mycin untreated human neuroblastomas correlates with advanced disease stage. *Science* **224**, 1121–1124 (1984).
3. H. Chen, H. Liu, G. Qing, Targeting oncogenic Myc as a strategy for cancer treatment. *Signal Transduct. Target. Ther.* **3**, 5 (2018).
4. A. J. Wolpaw, R. Bayliss, G. Buchel, C. V. Dang, M. Eilers, W. C. Gustafson, G. H. Hansen, N. Jura, S. Knapp, M. A. Lemmon, D. Levens, J. M. Maris, R. Marmorstein, S. J. Metallo, J. R. Park, L. Z. Penn, M. Rape, M. F. Roussel, K. M. Shokat, W. P. Tansey, K. A. Verba, S. M. Vos, W. A. Weiss, E. Wolf, Y. P. Mosse, Drugging the "Undruggable" MYCN oncogenic transcription factor: Overcoming previous obstacles to impact childhood cancers. *Cancer Res.* **81**, 1627–1632 (2021).
5. W. A. Weiss, K. Aldape, G. Mohapatra, B. G. Feuerstein, J. M. Bishop, Targeted expression of MYCN causes neuroblastoma in transgenic mice. *EMBO J.* **16**, 2985–2995 (1997).
6. C. A. Burkhart, A. J. Cheng, J. Madafiglio, M. Kavallaris, M. Mili, G. M. Marshall, W. A. Weiss, L. M. Khachigian, M. D. Norris, M. Haber, Effects of MYCN antisense oligonucleotide administration on tumorigenesis in a murine model of neuroblastoma. *J. Natl. Cancer Inst.* **95**, 1394–1403 (2003).
7. T. Otto, S. Horn, M. Brockmann, U. Eilers, L. Schuttrumpf, N. Popov, A. M. Kenney, J. H. Schulte, R. Beijersbergen, H. Christiansen, B. Berwanger, M. Eilers, Stabilization of N-Myc is a critical function of Aurora A in human neuroblastoma. *Cancer Cell* **15**, 67–78 (2009).
8. D. Xiao, M. Yue, H. Su, P. Ren, J. Jiang, F. Li, Y. Hu, H. Du, H. Liu, G. Qing, Polo-like kinase-1 regulates Myc stabilization and activates a feedforward circuit promoting tumor cell survival. *Mol. Cell* **64**, 493–506 (2016).
9. L. Wang, C. Chen, Z. Song, H. Wang, M. Ye, D. Wang, W. Kang, H. Liu, G. Qing, EZH2 depletion potentiates MYC degradation inhibiting neuroblastoma and small cell carcinoma tumor formation. *Nat. Commun.* **13**, 12 (2022).
10. C. Y. Lin, J. Loven, P. B. Rahl, R. M. Paranal, C. B. Burge, J. E. Bradner, T. I. Lee, R. A. Young, Transcriptional amplification in tumor cells with elevated c-Myc. *Cell* **151**, 56–67 (2012).
11. R. Zeid, M. A. Lawlor, E. Poon, J. M. Reyes, M. Fulciniti, M. A. Lopez, T. G. Scott, B. Nabet, M. A. Erb, G. E. Winter, Z. Jacobson, D. R. Polaski, K. L. Karlin, R. A. Hirsch, N. P. Munshi, T. F. Westbrook, L. Chesler, C. Y. Lin, J. E. Bradner, Enhancer invasion shapes MYCN-dependent transcriptional amplification in neuroblastoma. *Nat. Genet.* **50**, 515–523 (2018).
12. S. Venkatesh, J. L. Workman, Histone exchange, chromatin structure and the regulation of transcription. *Nat. Rev. Mol. Cell Biol.* **16**, 178–189 (2015).
13. V. M. Weake, J. L. Workman, Inducible gene expression: Diverse regulatory mechanisms. *Nat. Rev. Genet.* **11**, 426–437 (2010).
14. H. Kwak, J. T. Lis, Control of transcriptional elongation. *Annu. Rev. Genet.* **47**, 483–508 (2013).
15. S. R. Eberhardy, P. J. Farnham, Myc recruits P-TEFb to mediate the final step in the transcriptional activation of the cad promoter. *J. Biol. Chem.* **277**, 40156–40162 (2002).
16. S. Herold, J. Kalb, G. Buchel, C. P. Ade, A. Baluapuri, J. Xu, J. Koster, D. Solvie, A. Carstensen, C. Klotz, S. Rodewald, C. Schulein-Volk, M. Dobbelstein, E. Wolf, J. Molenaar, R. Versteeg, S. Walz, M. Eilers, Recruitment of BRCA1 limits MYCN-driven accumulation of stalled RNA polymerase. *Nature* **567**, 545–549 (2019).
17. D. Papadopoulos, D. Solvie, A. Baluapuri, T. Endres, S. A. Ha, S. Herold, J. Kalb, C. Giansanti, C. Schülein-Völk, C. P. Ade, C. Schneider, A. Gaballa, S. Vos, U. Fischer, M. Dobbelstein, E. Wolf, M. Eilers, MYCN recruits the nuclear exosome complex to RNA polymerase II to prevent transcription-replication conflicts. *Mol. Cell* **82**, 159–176.e12 (2022).
18. G. Qing, B. Li, A. Vu, N. Skuli, Z. E. Walton, X. Liu, P. A. Mayes, D. R. Wise, C. B. Thompson, J. M. Maris, M. D. Hogarty, M. C. Simon, ATF4 regulates *MYC*-mediated neuroblastoma cell death upon glutamine deprivation. *Cancer Cell* **22**, 631–644 (2012).
19. N. Fong, K. Brannan, B. Erickson, H. Kim, M. A. Cortazar, R. M. Sheridan, T. Nguyen, S. Karp, D. L. Bentley, Effects of transcription elongation rate and Xrn2 exonuclease activity on RNA polymerase II termination suggest widespread kinetic competition. *Mol. Cell* **60**, 256–267 (2015).
20. Z. Luo, C. Lin, A. Shilatifard, The super elongation complex (SEC) family in transcriptional control. *Nat. Rev. Mol. Cell Biol.* **13**, 543–547 (2012).
21. E. Poon, T. Liang, Y. Jamin, S. Walz, C. Kwok, A. Hakkert, K. Barker, Z. Urban, K. Thway, R. Zeid, A. Hallsworth, G. Box, M. E. Ebus, M. P. Licciardello, Y. Sbirkov, G. Lazaro, E. Calton, B. M. Costa, M. Valenti, A. D. H. Brandon, H. Webber, N. Tardif, G. S. Almeida, R. Christova, G. Boysen, M. W. Richards, G. Barone, A. Ford, R. Bayliss, P. A. Clarke, J. De Bono, N. S. Gray, J. Blagg, S. P. Robinson, S. A. Eccles, D. Zheleva, J. E. Bradner, J. Molenaar, I. Vivanco, M. Eilers, P. Workman, C. Y. Lin, L. Chesler, Orally bioavailable CDK9/2 inhibitor shows mechanism-based therapeutic potential in MYCN-driven neuroblastoma. *J. Clin. Invest.* **130**, 5875–5892 (2020).
22. A. Baluapuri, J. Hofstetter, N. Dudvarski Stankovic, T. Endres, P. Bhandare, S. M. Vos, B. Adhikari, J. D. Schwarz, A. Narain, M. Vogt, S.-Y. Wang, R. Duster, L. A. Jung, J. T. Vanselow, A. Wiegering, M. Geyer, H. M. Maric, P. Gallant, S. Walz, A. Schlosser, P. Cramer, M. Eilers, E. Wolf, MYC recruits SPT5 to RNA polymerase II to promote processive transcription elongation. *Mol. Cell* **74**, 674–687 e11 (2019).
23. K. Liang, E. R. Smith, Y. Aoi, K. L. Stoltz, H. Katagi, A. R. Woodfin, E. J. Rendleman, S. A. Marshall, D. C. Murray, L. Wang, P. A. Ozark, R. K. Mishra, R. Hashizume, G. E. Schiltz, A. Shilatifard, Targeting processive transcription elongation via SEC disruption for MYC-induced cancer therapy. *Cell* **175**, 766–779 e17 (2018).
24. F. Lamers, L. Schild, I. J. den Hartog, M. E. Ebus, E. M. Westerhout, I. Ora, J. Koster, R. Versteeg, H. N. Caron, J. J. Molenaar, Targeted BCL2 inhibition effectively inhibits neuroblastoma tumour growth. *Eur. J. Cancer* **48**, 3093–3103 (2012).
25. D. R. Carter, J. Murray, B. B. Cheung, L. Gamble, J. Koach, J. Tsang, S. Sutton, H. Kalla, S. Syed, A. J. Gifford, N. Issaeva, A. Biktasova, B. Atmadibrata, Y. Sun, N. Sokolowski, D. Ling, P. Y. Kim, H. Webber, A. Clark, M. Ruhle, B. Liu, A. Oberthuer, M. Fischer, J. Byrne, F. Saletta, M. Thwe Ie, A. Purmal, G. Haderski, C. Burkhart, F. Speleman, K. De Preter, A. Beckers, D. S. Ziegler, T. Liu, K. V. Gurova, A. V. Gudkov, M. D. Norris, M. Haber, G. M. Marshall, Therapeutic targeting of the MYC signal by inhibition of histone chaperone FACT in neuroblastoma. *Sci. Transl. Med.* **7**, 312ra176 (2015).
26. H. Takahashi, T. J. Parmely, S. Sato, C. Tomomori-Sato, C. A. Banks, S. E. Kong, H. Szutorisz, S. K. Swanson, S. Martin-Brown, M. P. Washburn, L. Florens, C. W. Seidel, C. Lin, E. R. Smith, A. Shilatifard, R. C. Conaway, J. W. Conaway, Human mediator subunit MED26 functions as a docking site for transcription elongation factors. *Cell* **146**, 92–104 (2011).
27. C. Guo, Z. Che, J. Yue, P. Xie, S. Hao, W. Xie, Z. Luo, C. Lin, ENL initiates multivalent phase separation of the super elongation complex (SEC) in controlling rapid transcriptional activation. *Sci. Adv.* **6**, eaay4858 (2020).
28. Z. Qiu, L. Zhao, J. Z. Shen, Z. Liang, Q. Wu, K. Yang, L. Min, R. C. Gimple, Q. Yang, S. Bhargava, C. Jin, C. Kim, D. Hinz, D. Dixit, J. A. Bernatchez, B. C. Prager, G. Zhang, Z. Dong, D. Lv, X. Wang, L. J. Y. Kim, Z. Zhu, K. A. Jones, Y. Zheng, X. Wang, J. L. Siqueira-Neto, L. Chavez, X.-D. Fu, C. Spruck, J. N. Rich, Transcription elongation machinery is a druggable dependency and potentiates immunotherapy in glioblastoma stem cells. *Cancer Discov.* **12**, 502–521 (2022).
29. B. J. Lestini, K. C. Goldsmith, M. N. Fluchel, X. Liu, N. L. Chen, B. Goyal, B. R. Pawel, M. D. Hogarty, Mcl1 downregulation sensitizes neuroblastoma to cytotoxic chemotherapy and small molecule Bcl2-family antagonists. *Cancer Biol. Ther.* **8**, 1587–1595 (2009).
30. K. Liang, A. R. Woodfin, B. D. Slaughter, J. R. Unruh, A. C. Box, R. A. Rickels, X. Gao, J. S. Haug, S. L. Jaspersen, A. Shilatifard, Mitotic Transcriptional activation: Clearance of actively engaged Pol II via transcriptional elongation control in mitosis. *Mol. Cell* **60**, 435–445 (2015).
31. K. F. Cho, T. C. Branon, N. D. Udeshi, S. A. Myers, S. A. Carr, A. Y. Ting, Proximity labeling in mammalian cells with TurboID and split-TurboID. *Nat. Protoc.* **15**, 3971–3999 (2020).
32. T.-C. Chou, Drug combination studies and their synergy quantification using the Chou-Talalay method. *Cancer Res.* **70**, 440–446 (2010).
33. Y. Perez-Riverol, J. Bai, C. Bandla, D. García-Seisdedos, S. Hewapathirana, S. Kamatchinathan, D. J. Kundu, A. Prakash, A. Frericks-Zipper, M. Eisenacher, M. Walzer, S. Wang, A. Brazma, J. A. Vizcaíno, The PRIDE database resources in 2022: A hub for mass spectrometry-based proteomics evidences. *Nucleic Acids Res.* **50**, D543–d552 (2022).

Acknowledgments: We thank the members of the Qing, Liang, and Liu laboratories for tremendous technical support and critical reading of the manuscript. We thank the Core Facility of Medical Research Institute at Wuhan University for histological analysis and the Research Center for Medicine and Structural Biology of Wuhan University for proteomic assistance.
Funding: This study was supported by grants from National Key R&D Program of China (2021YFA1100501 to G.Q. and 2022YFA1103200 to H.L.), National Natural Science Foundation of China (82230092 and 81830084 to G.Q., 82172641 to K.L., and 81970152 to H.L.), National Science Foundation for Distinguished Young Scholar (81725013 to G.Q. and 82025003 to H.L.), National Natural Science Foundation Excellent Young Scientists Fund (82122006 to K.L.), and Hubei Provincial Natural Science Fund for Creative Research Groups (2021CFA003 to H.L.).
Author contributions: G.Q., K.L., and H.L. conceived ideas and designed the study. G.Q., K.L., and H.L. supervised the study. H.L., K.L., G.Q., and D.W. wrote the manuscript. D.W. and H.W.

performed cell-based experiments and sequencing analysis. D.W., L.W., R.H., and T.X. conducted animal experiments. Z.Y. and D.W. analyzed the sequencing data. T.L. and R.X. performed TurboID and co-IP mass spectrometry analysis. R.D. provided neuroblastoma patient primary tumors. **Competing interests:** The authors declare that they have no competing interests. **Data and materials availability:** The raw data of RNA-seq, TT-seq, and ChIP-seq reported in this study were deposited in the National Center for Biotechnology Information's Gene Expression Omnibus [https://www.ncbi.nlm.nih.gov/geo/ (GSE199086)]. The mass spectrometry proteomics data have been deposited to the ProteomeXchange Consortium via the PRIDE (*33*) partner repository with the dataset identifier PXD039332. All data needed to evaluate the conclusions in the paper are present in the paper and/or the Supplementary Materials.

Submitted 3 October 2022
Accepted 28 February 2023
Published 29 March 2023
10.1126/sciadv.adf0005